Biosensors and Bioelectronics 237 (2023) 115498

Contents lists available at ScienceDirect

Biosensors and Bioelectronics

journal homepage: www.elsevier.com/locate/bios

Surface-acoustic-wave-driven graphene plasmonic sensor for fingerprinting ultrathin biolayers down to the monolayer limit

Raúl Izquierdo-López *, Rajveer Fandan, Alberto Boscá, Fernando Calle, Jorge Pedrós **

Instituto de Sistemas Optoelectrónicos y Microtecnología, Departamento de Ingeniería Electrónica, E.T.S.I. de Telecomunicación, Universidad Politécnica de Madrid, Av. Complutense 30, Madrid, 28040, Spain

ARTICLE INFO

Keywords:
Surface plasmon polariton
Surface enhanced infrared absorption (SEIRA)
Vibrational fingerprint
Surface acoustic wave (SAW)
Fano resonance

ABSTRACT

Surface plasmon polaritons in graphene can enhance the performance of mid-infrared spectroscopy, which is key for the study of both the composition and the conformation of organic molecules via their vibrational resonances. In this paper, a plasmonic biosensor using a graphene-based van der Waals heterostructure on a piezoelectric substrate is theoretically demonstrated, where far-field light is coupled to surface plasmon-phonon polaritons (SPPPs) through a surface acoustic wave (SAW). The SAW creates an electrically-controlled virtual diffraction grating, suppressing the need for patterning the 2D materials, that limits the polariton lifetime, and enabling differential measurement schemes, which increase the signal-to-noise ratio and allow a quick commutation between reference and sample signals. A transfer matrix method has been used for simulating the SPPPs propagating in the system, which are electrically tuned to interact with the vibrational resonances of the analytes. Furthermore, the analysis of the sensor response with a coupled oscillators model has proven its capability of fingerprinting ultrathin biolayers, even when the interaction is too weak to induce a Fano interference pattern, with a sensitivity down to the monolayer limit, as tested with a protein bilayer or a peptide monolayer. The proposed device paves the way for the development of advanced SAW-assisted lab-on-chip systems combining the existing SAW-mediated physical sensing and microfluidic functionalities with the chemical fingerprinting capability of this novel SAW-driven plasmonic approach.

1. Introduction

The mid-infrared range (3–20 μm) is of great importance in spectroscopy since it contains the vibrational fingerprint of molecules, that is the set of absorption resonances related to the molecular bonds that uniquely identify a substance. Furthermore, the position and relative intensity of these resonances can be used to infer the conformation of the molecules. In the case of proteins and peptides, the mid-infrared spectrum gives access to their secondary structure as well as to local interactions, adsorption or binding processes in a label-free manner (Barth, 2007; López-Lorente and Mizaikoff, 2016). However, sensing ultrathin biolayers is challenging because of the low absorption cross-section resulting from the strong size mismatch between free radiation (wavelength ~ μm) and biomolecules (size ~ nm). This limitation can be overcome with surface plasmon polaritons (SPPs), confined modes at the surface of a conductor originating from the coupling of the radiation with collective electron excitations, which provide higher momentum and smaller mode volume than free radiation. This turns into a higher local electric field intensity that strengthens light-matter interactions at the nanoscale, being the principle of surface-enhanced infrared absorption (SEIRA) spectroscopy (Adato and Altug, 2013; Neuman et al., 2015; Yi et al., 2020).

Graphene has emerged as a prominent SEIRA platform supporting SPPs in the mid-infrared range, providing much greater confinement factors than metals, due to its 2D nature, while maintaining long lifetimes (Hu et al., 2016; Li et al., 2014; Rodrigo et al., 2015; Lee et al., 2019). Moreover, as opposed to metals, its carrier density can be tuned electrically, allowing to modulate the SPP frequency. On the other hand, charge carriers in graphene can interact with the surface phonons of polar substrates through the Fröhlich coupling, leading to hybridization into surface plasmon-phonon polaritons (SPPPs). This hybridization can increase the polariton lifetime when graphene is stacked with other 2D materials such as hexagonal boron nitride (h-BN). (Brar et al., 2014; Fandan et al., 2018).

* Corresponding author.
** Corresponding author.
E-mail addresses: raul.izquierdo@upm.es (R. Izquierdo-López), j.pedros@upm.es (J. Pedrós).

https://doi.org/10.1016/j.bios.2023.115498
Received 16 January 2023; Received in revised form 14 May 2023; Accepted 23 June 2023
Available online 26 June 2023

Coupling light into graphene SPPs (or SPPPs) typically requires either complex near-field techniques (Fei et al., 2011; Zhang et al., 2022) or patterning nanostructures as diffraction gratings (Brar et al., 2013; Fang et al., 2014; Ju et al., 2011), being the latter restricted to the excitation of localized plasmons where edge scattering reduces the plasmon lifetime. However, surface acoustic waves (SAWs) have been shown to couple far-field light into propagating polaritons (Ruppert et al., 2010; Schiefele et al., 2013) without the need of patterning the material, since the dynamic local strain of the SAW (Fandan et al., 2020) generates a sinusoidal surface deformation that acts as a virtual diffraction grating. Moreover, the on-chip transducer generating the SAW allows to switch electrically the polariton launching, thus facilitating the implementation of differential sensing schemes without the need of additional reference devices.

The combination of metal-based surface plasmon resonance (SPR) structures operating in the visible range with SAW devices has been already explored for lab-on-chip (LOC) applications aiming at the simultaneous measurement of the refractive index and the mass of an adsorbed substance (Friedt et al., 2004; Friedt and Francis, 2016) or the inclusion of SAW-driven microfluidic capabilities, such as the streaming of a droplet or the mixing of its fluid for enhanced binding kinetics (Galopin et al., 2007; Renaudin et al., 2010; Sonato et al., 2016). However, none of these systems are capable of fingerprinting or providing chemical information about the substance but only sensing some of its physical properties, as they operate in the visible range. Moreover, they are mostly based on the coupling of the light by means of a prism, an approach that cannot be used for graphene in the mid-infrared range as the required value of the refractive index of the prism would be beyond that of the existing materials (Nikitin et al., 2014).

In this work, we propose a SAW-driven plasmonic biosensor using a graphene-based van der Waals heterostructure on a piezoelectric substrate for fingerprinting ultrathin biolayers. The SPPPs propagating in the unpatterned 2D system, operating in the mid-infrared range, interact with the vibrational resonances of the analytes providing sensitivity down to the monolayer (ML) limit. The performance of the proposed biosensor has been studied theoretically using various analytes, including ultrathin films of an organic polymer presenting strong absorption lines as well as significant biological substances with weaker and broader resonances such as a protein bilayer and peptide MLs.

2. Methods

The proposed biosensor consists of a two-port SAW resonator fabricated on a piezoelectric substrate. A 2D system formed by two double layer graphene (DLG) stacks separated by h-BN (DLG/h-BN/DLG) is then placed in between the interdigital transducers (IDTs), so that a standing SAW is established across the van der Waals heterostructure. The SAW acts as a virtual diffraction grating providing the extra momentum necessary to couple far field TM-polarized light into the SPPPs supported by the 2D system. A quantum cascade laser can be used as the mid-infrared light source, since it permits to deliver coherent and polarized light with high spectral power density (Schwaighofer et al., 2017) concentrated in the active region of the sensor. The analyte is finally deposited on top forming an ultrathin layer. The sensor monitors the plasmonic response of the whole structure, which is modified by the coating, allowing the identification or fingerprinting of the analyte and the quantification of its thickness down to the single ML limit. Fig. 1(a) shows schematically the concept of the SAW-assisted plasmonic biosensor that will be described in detail in this study. Here, aluminum nitride (AlN) has been chosen as the piezoelectric substrate since a buried gate can be easily fabricated during the epitaxial growth or sputtering deposition of the material in the form of a AlN/Al/AlN stack. This Al electrode allows to bias both DLGs in the DLG/h-BN/DLG system, as shown in Fig. 1(b), facilitating their gate doping and thus the electrical tuning of the energy of the SPPPs. The use of DLGs, providing each of them twice the Fermi energy of a single layer graphene (SLG) (Rodrigo et al., 2017), along with the hybridization of the graphene plasmons with the h-BN phonons, permits the modulation of the dispersion of the resulting SPPPs so that the whole mid-infrared fingerprinting region can be accessed.

A transfer matrix method (TMM) has been used to evaluate the Fresnel reflection and transmission coefficients of the sensor structure. The absorption of light is given by the imaginary part of the reflection coefficient, so that the poles of $\mathrm{Im}[r_{TM}(k,\omega)]$ provide the dispersion curve of the SPPPs of the material structure. The TMM just requires the permittivity of each individual dielectric layer as input, whereas the graphene layers are considered as a surface conductivity at the interface in between two dielectric layers (Fandan et al., 2018; Schiefele et al., 2013; Zhan et al., 2013). h-BN is an anisotropic material with two reststrahlen bands defined by its two infrared active phonon modes: the in-plane ($\|$) A_{2u} phonon modes, with frequencies $\omega_{TO,\|} = 0.096$ eV and $\omega_{LO,\|} = 0.102$ eV, and the out-of-plane ($\perp$) E_{1u} phonon modes, with frequencies $\omega_{TO,\perp} = 0.169$ eV and $\omega_{LO,\perp} = 0.199$ eV. The frequency-dependent permittivity of h-BN has been modelled as (Dai et al., 2014)

$$\epsilon_{h-BN,k}(\omega) = \epsilon_{\infty,k}\left[1 + \frac{\omega_{LO,k}^2 - \omega_{TO,k}^2}{\omega_{TO,k}^2 - i\omega\gamma_k - \omega^2}\right], \quad (1)$$

where $k = \|, \perp$, $\epsilon_{\infty,\|} = 2.95$ and $\epsilon_{\infty,\perp} = 4.87$ are the high-frequency dielectric constants, and $\gamma_\| = 0.49$ meV and $\gamma_\perp = 0.62$ meV are the

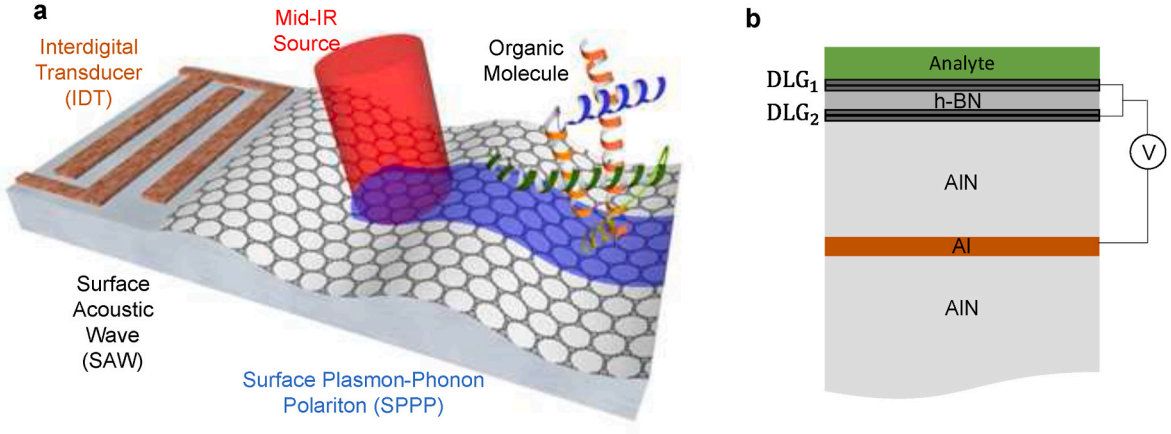

Fig. 1. Schematics of the SAW-driven plasmonic biosensor proposed. (a) 3D layout of the device and (b) cross section of the material system composed of a van der Waals heterostructure on top of an AlN substrate with a buried Al gate that is used to bias the top and bottom double layer graphene (DLG) stacks.

damping rates.

AlN is only slightly anisotropic compared to h-BN, so here, for simplicity, it is assumed to present an isotropic behaviour with a unique reststrahlen band located between $\omega_{TO} = 0.083$ eV and $\omega_{LO} = 0.111$ eV. The frequency-dependent permittivity of AlN has been modelled as (Kazan et al., 2009)

$$\epsilon_{AlN}(\omega) = \epsilon_\infty + (\epsilon_0 - \epsilon_\infty)\frac{\omega_{TO}^2}{\omega_{TO}^2 - i\omega\gamma - \omega^2}, \tag{2}$$

where $\epsilon_0 = 7.37$ and $\epsilon_\infty = 3.93$ are the static and high-frequency dielectric constants, respectively, and $\gamma = 0.64$ meV is the damping rate.

The frequency-dependent conductivity of graphene has been calculated as

$$\sigma(\omega) = \frac{i|E_F|e^2}{\pi\hbar^2(\omega + i/\tau)}, \tag{3}$$

where E_F is the Fermi energy and τ is the electron relaxation time. In this work, $\tau = 0.4$ ps has been assumed, which corresponds with a carrier mobility value of $\mu = 10000$ cm^{2}V^{-1}s^{-1}.

The sensor performance has been evaluated considering different analytes, including ultrathin films of the polymer 4,4′-bis(N-carbazolyl)-1,1′-biphenyl (CBP), the protein bilayer formed by the recombinant protein A/G and the goat anti-mouse immunoglobulin G (IgG) (A/G-IgG), and MLs of the peptide valine gramicidine A (VGA). In all cases, their frequency-dependent permittivity have been modelled as a sum of Lorentz oscillators, each of them representing the resonance of a characteristic chemical group, as

$$\epsilon_{analyte}(\omega) = \epsilon_\infty + \sum_{k=1}^{N}\frac{h_k^2}{\omega_k^2 - i\omega\gamma_k - \omega^2}, \tag{4}$$

where h_k, ω_k, and γ_k are the amplitude, frequency, and damping rate of each of the N resonances, respectively, and ϵ_∞ is the high-frequency dielectric constant of the material. The list of these parameters and the resulting plot of the permittivity for each of these analytes can be found in Table S1 and Figs. S1–S3, respectively, of the Supplementary Information.

Light coupled to the polariton in the sensor can be calculated as the light diffracted into the surface of the heterostructure by a sinusoidal surface. Incident light with wavevector ($k_{||,0}$, $k_{z,0}$) is scattered into the various diffraction orders ($k_{||,m}$, $k_{z,m}$) with

$$k_{||,m} = \frac{\omega}{c}sin\theta + m\frac{2\pi}{\lambda_{SAW}}, \tag{5}$$

$$k_{zm} = \sqrt{(\omega/c)^2 - k_{\|m}^2}, \tag{6}$$

where θ is the angle of off-normal incidence, m is an integer, and λ_{SAW} is the SAW wavelength (i.e. the period of the IDT). The wavevector of the polariton is hence mainly governed by λ_{SAW}, as $(\omega/c)sin\theta \ll 2\pi/\lambda_{SAW}$. Here, for simplicity, normal incidence ($\theta = 0$) has been assumed. The mth order diffraction of light at a surface with a sinusoidal corrugation is then given as (Lean, 1973; Schiefele et al., 2013)

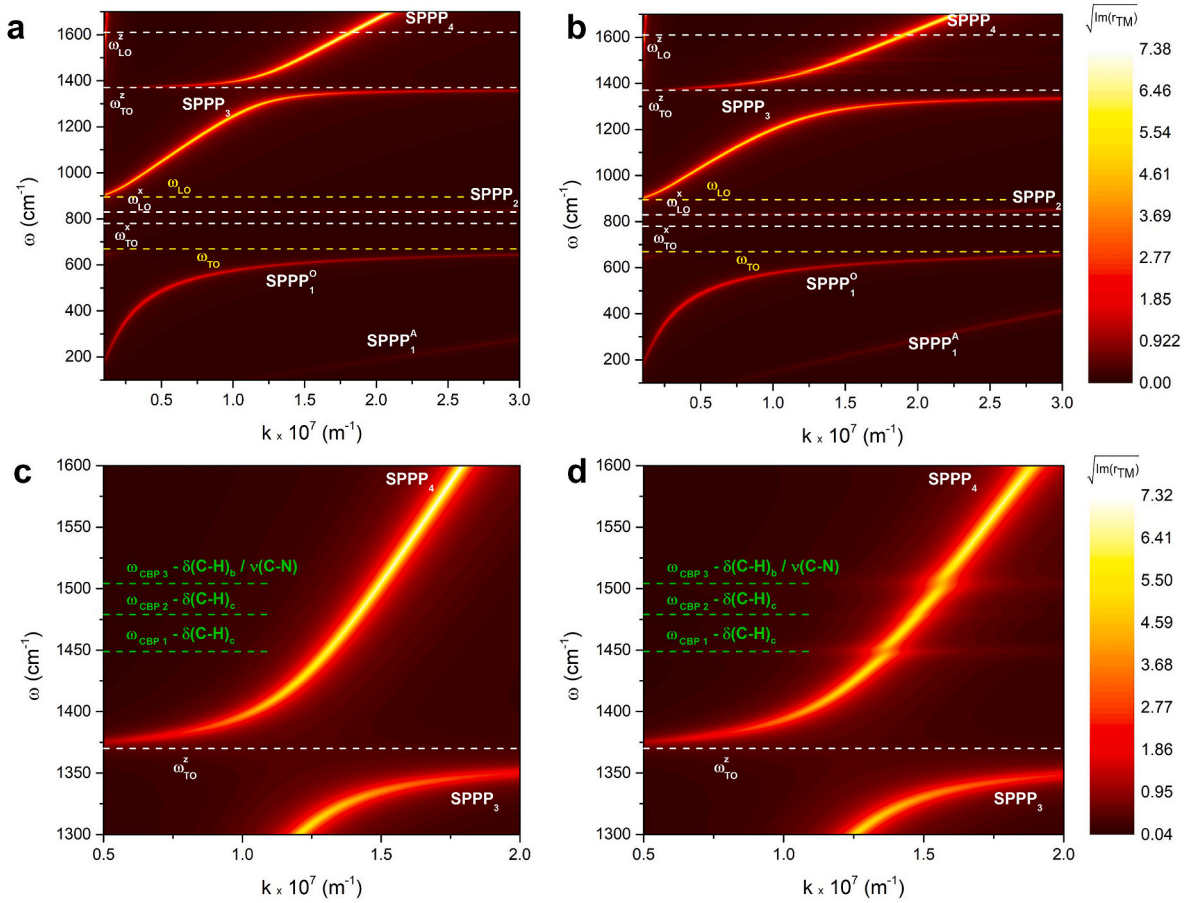

Fig. 2. Dispersion of the surface plasmon-phonon polaritons $SPPP_i$ for the DLG/h-BN/DLG/AlN/Al/AlN system without (a),(c) and with (b),(d) a 5 nm-thick CBP layer on top. (c) and (d) show a magnified view of the CBP fingerprint region in (a) and (b), respectively. White and yellow dashed lines indicate the optical phonon frequencies of h-BN and AlN respectively, whereas green dashed lines are displayed at the frequencies of the vibrational resonances of CBP. The Fermi energy is $E_F =$ 0.4 eV for all graphene sheets and the h-BN layer is 2 nm thick.

$$I^m = \left| r_{TM} J_m(2k_{z0}\delta) \left[1 + \frac{m\pi}{\lambda_{SAW} k_{zm}} \frac{1 + r_{TM}}{r_{TM}} \right] \right|^2, \quad (7)$$

where J_m is the Bessel function of order m and δ is the SAW amplitude. In this work $\delta = 1$ nm has been considered. Since $k_{z0}\delta \ll 1$, $|J_m(2k_{z0}\delta)|^2 \approx (k_{z0}\delta)^{2m}$ and the diffraction can be restricted to the first order.

3. Results and discussion

Fig. 2 shows the dispersion curves for the bare DLG/h-BN/DLG/AlN/Al/AlN sensor heterostructure, Fig. 2(a) and (c), and coated by a 5 nm-thick CBP layer, Fig. 2(b) and (d). Here, the AlN top layer has been chosen to have a thickness of 500 nm. This ensures that the Al buried gate does not contribute to the dispersion, allowing us to reduce the AlN/Al/AlN stack in the calculations to just an AlN substrate (see Fig. S4 of the Supplementary Information). The bare heterostructure, Fig. 2(a), supports four surface plasmon-phonon polaritons ($SPPP_i$, $i = 1$–4) arising from the hybridization of the graphene surface plasmon and the optical phonons of the h-BN interlayer and the AlN substrate. Furthermore, the two DLGs separated by the h-BN spacer give rise to optical ($SPPP_i^O$) and acoustic ($SPPP_i^A$) modes, corresponding, respectively, to the in-phase and out-of-phase coupling of the plasmons in both DLGs. Although only the first acoustic mode $SPPP_1^A$ appears in Fig. 2(a), higher energy acoustic modes are found at higher wavevectors, as discussed in Section 3 of the Supplementary Information. CBP presents three vibrational resonances within the upper reststrahlen band of h-BN, that appear as faint features in Fig. 2(b) interacting with the $SPPP_4$ mode. Resonances at $\omega_{CBP_1} = 1449$ cm^{-1} and $\omega_{CBP_2} = 1479$ cm^{-1} are due to deformation modes of the C–H bond located mainly in the carbazole group (δ(C–H)$_c$), whereas resonance at $\omega_{CBP_3} = 1504$ cm^{-1} originates from the deformation mode of the C–H bond at the biphenyl group (δ(C–H)$_b$) and the stretching mode of the C–N bond (ν(C–N)) (Huck et al., 2014). The comparison of the magnified view of the upper reststrahlen band of h-BN with and without the CBP analyte, depicted in Fig. 2(d) and (c) respectively, clearly shows anticrossing features proving the coupling between these vibrational resonances and the $SPPP_4$ mode that allows the biosensor fingerprinting the CBP.

Fig. 3 describes the operation principle of the DLG/h-BN/DLG/AlN/Al/AlN sensor for fingerprinting the vibrational resonances of CBP. On the one hand, the deposition of CBP layers of increasing thickness leads to a polariton frequency shift induced by the associated change in the dielectric environment, as depicted in Fig. 3(a) around the vibration δ(C–H)$_c$. However, this mechanism only permits to infer the effective refractive index of the analyte (Zhao et al., 2013) but lacks specificity. On the other hand, the interaction between the polariton and the vibrational resonance of CBP leads to small dips at the tails of the spectra. Nevertheless, these features are not strong enough to provide the required sensor sensitivity. The specificity, and hence the fingerprinting capability, together with the enhanced sensitivity of the proposed sensor rely on the tuning of the Fermi level of the DLGs via a gate bias, so that the polariton is continuously forced to overlap with the vibrational resonance of CBP, as shown in Fig. 3(b) for the case of the vibration δ(C–H)$_c$. In this configuration, as the thickness of the analyte layer is increased, two different regimes can be distinguished. Initially, a broadening of the extinction peak is observed that gradually turns into the emergence of a transparency window within the extinction peak at around the frequency of the vibrational transition.

This latter transparency-window regime has been previously reported in different types of polaritonic systems such as metallic antennas (Vogt et al., 2015) and graphene (Hu et al., 2016; Li et al., 2014) or h-BN (Autore et al., 2018) nanoribbon arrays, among others (Kamenetskii et al., 2018). Nevertheless, the interaction between the electric field of the polariton and the dipole associated with the molecular vibration is not always large enough to reach this regime, as can be seen in Fig. 3(b) for a CBP thickness below 1 nm. The possibility of tuning the frequency response of the sensor not only allows to compensate for the frequency shift induced by the addition of the analyte layer but also to target different vibrational resonances with the same device. This is illustrated in Fig. 3(c), where the Fermi energy is varied for a fixed CBP layer thickness in order to probe the distinct vibrational resonances that unambiguously fingerprint the analyte. This information can be complemented with the amount (thickness) of analyte being tested, obtained from the frequency shift of the extinction peak before any Fermi level correction is made. Furthermore, the SAW itself will also suffer from a frequency shift induced by the mass loading from the analyte, that can be detected monitoring the passband of the SAW device. Thus, these two signals can be used for autocalibration.

In the transparency-window regime of the sensor, the molecule-polariton interaction can be quantified by considering either the depth or the width of the transparency window. However, this cannot be applied to the broadening regime of the sensor, despite the molecule-polariton interaction is already strong enough to modify the spectrum, as seen in Fig. 3(b). In order to find a parameter suitable to quantify this interaction consistently across both regimes, the electric fields of both the polariton and the vibrational resonance have been modelled. A coupled oscillator model (COM), adapted from (Liu et al., 2009) to account for a system with two oscillators interacting with far-field light, has been used to simulate the biosensor response. This model is described by the following equation system.

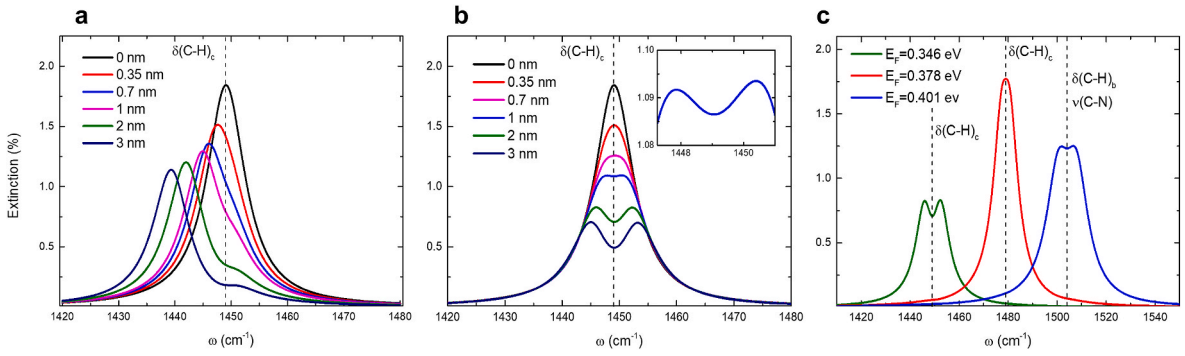

Fig. 3. (a) Evolution of the extinction of the sensor for a CBP layer thickness ranging from 0 (no layer) up to 3 nm. The polariton wavevector is $k_p = 1.52 \cdot 10^7$ m^{-1} ($\lambda_{SAW} \approx 400$ nm) and the Fermi energy of the graphene layers at the top and bottom DLGs is set to $E_F = 0.339$ eV. (b) Evolution of the extinction of the sensor considering the same CBP thickness values as in (a) but adjusting the Fermi levels to compensate for the frequency shift ($k_p = 1.52 \cdot 10^7$ m^{-1} and $E_F = 0.339$, 0.341, 0.342, 0.343, 0.347 and 0.350 eV for CBP layer thickness ranging from 0 to 3 nm). Two different regimes can be observed when changing the analyte thickness (see main text). The inset shows a magnified view of the 1 nm-thickness curve around the resonance frequency. (c) Extinction plots of the sensor covered by a 2 nm-thick CBP layer for $k_p = 1.52 \cdot 10^7$ m^{-1} and different E_F values to match the three resonances of CBP, as indicated by the black dashed lines.

$$\begin{aligned} \ddot{x}_1 + \gamma_1\dot{x}_1 + \omega_1^2 x_1 + \kappa\dot{x}_2 &= F_1\exp(-i\omega t) \\ \ddot{x}_2 + \gamma_2\dot{x}_2 + \omega_2^2 x_2 - \kappa\dot{x}_1 &= F_2\exp(-i\omega t) \end{aligned} \tag{8}$$

where, x_i, γ_i, ω_i and F_i refer to the amplitude, damping, resonance frequency and driving force, respectively, of the harmonic oscillators and κ denotes the coupling coefficient between them. Hereafter, subscripts 1 and 2 will denote, respectively, the polariton and the vibrational resonance. The driving force of each individual oscillator can be understood as a measure of the direct interaction of each of them with the far field light.

In order to compare the results of the COM with those from the TMM simulations, a simplified structure comprised of, from bottom to top, an AlN substrate, a SLG, and a 2-nm-thick CBP layer (CBP/SLG/AlN) has been considered. Moreover, only one of the vibrational resonances of CBP has been addressed. This reduces the number of interacting resonances involved in the process, simplifying the analysis while maintaining all the physical mechanisms involved. Thus, the simplified structure retains 3 resonances: the optical phonon of AlN ω_{TO} at 669 cm^{-1}, the vibrational resonance of CBP ω_{CBP_2} at 1479 cm^{-1}, and the graphene plasmon ω_{pl}, which follows the dispersion equation (Low and Avouris, 2014)

$$\omega_{pl}(k) = \sqrt{\frac{2\alpha E_F c k}{\hbar\epsilon_{eff}}}, \tag{9}$$

where $\alpha \sim 1/137$ is the fine structure constant, E_F is the Fermi energy of the graphene layer, c is the speed of light in vacuum, $\epsilon_{eff} = \frac{\epsilon_s+1}{2}$ is the effective permittivity of the substrate and the air, and k is the wavevector. These three resonances define a COM matrix. The 3 × 3 Hamiltonian will have 3 eigenvalues (3 branches in the dispersion). Assuming there is no coupling between the CBP resonance and the AlN phonon because of their large difference in frequency, this matrix reads

$$\widehat{M} = \begin{pmatrix} \omega_{pl} & g_{ph} & g_{CBP} \\ g_{ph} & \omega_{TO} & 0 \\ g_{CBP} & 0 & \omega_{CBP_2} \end{pmatrix}, \tag{10}$$

where g_{ph} and g_{CBP} are the coupling coefficients between the graphene plasmon and the AlN phonon and the resonance of the CBP, respectively. These coefficients can be obtained from the energy difference between the resonances, see (Fandan et al., 2021).

Fig. 4(a) compares the results from the TMM and the COM, showing a very good agreement for the calculation of the dispersion, both predicting the anticrossing point between the vibrational resonance and the SPPP, which leads to an upper (U) and a middle (M) branch. The lower (L) branch, which is not shown in the figure, would appear just below the other anticrossing point between the plasmon and the AlN TO phonon. Fig. 4(b) displays the squared modulus of the components of the eigenvector associated to each of the eigenvalues (branches of the dispersion), $|X_i|^2$, in Fig. 4(a). The relative weights of each component represent the plasmonic-phononic-vibrational character of the polariton. These weights affect, for instance, the bandwidth of the polariton resonance, which will be given by the weighted sum of the bandwidths of the plasmon, the phonon, and the vibrational resonances. In terms of lifetimes, τ_i, this is expressed as $\frac{1}{\tau_p} = |X_{pl}|^2\frac{1}{\tau_{pl}} + |X_{ph}|^2\frac{1}{\tau_{ph}} + |X_{CBP}|^2\frac{1}{\tau_{CBP}}$. The M branch is fully plasmonic-phononic until the vicinity of the anticrossing, where the vibrational resonance starts to hybridize with the SPPP. Conversely, the U branch has a pure vibrational nature for wavevectors below the anticrossing and hybridizes with the SPPP above it. It can be noted that the contribution of the phonon decreases with increasing wavevector in both M and U branches, as they move farther away from the energy of the phonon.

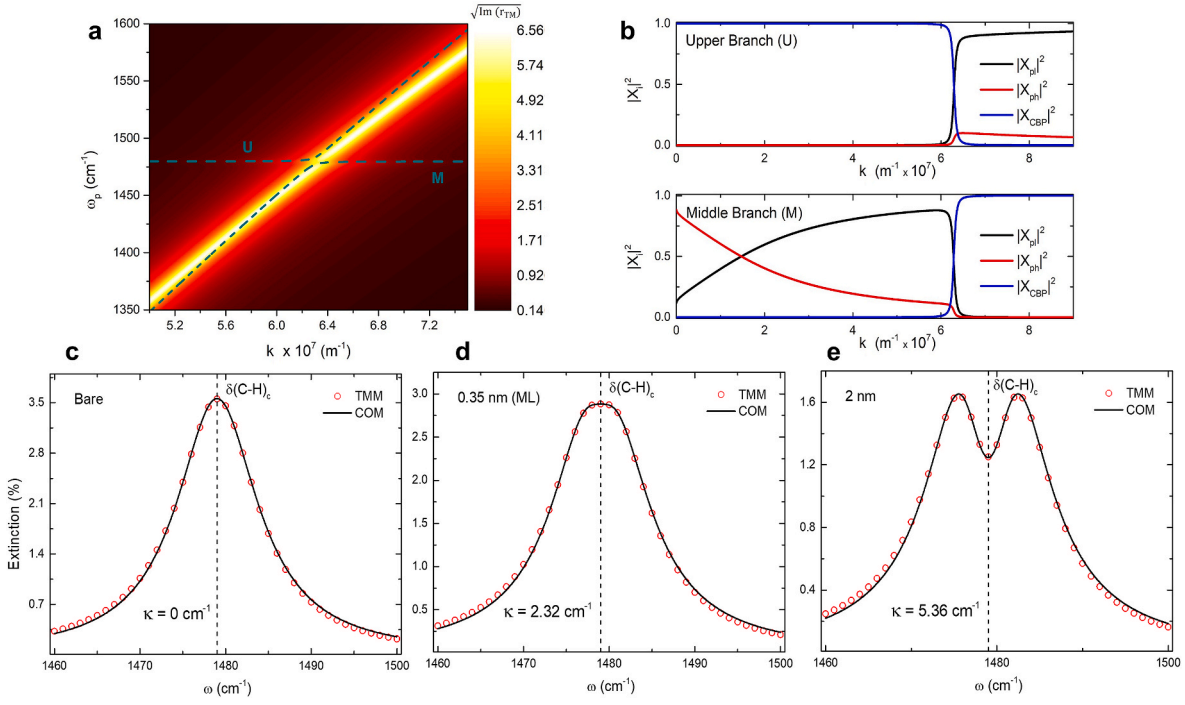

Fig. 4. (a) Detail of the polariton dispersion of the CBP/SLG/AlN system around the vibration of the carbazole group of CBP (δ(C–H)$_c$ at 1479 cm^{-1}) calculated from the TMM (colorbar scale) and the COM (turquoise dashed lines) showing the upper (U) and middle (M) branches. (b) Eigenvectors of the COM Hamiltonian corresponding to each of the eigenvalues represented in (a). Different colours represent each of the components of the eigenvector, linked to the phononic/plasmonic/vibrational character of the polariton. In (c), (d) and (e) the extinction of the CBP/SLG/AlN system calculated from the TMM (red circles) is plotted along with the COM model fitting function (black curves) for CBP thickness values of 0 nm (bare), 0.35 nm (1 ML) and 2 nm at a polariton wavevector $k_p = 6.29 \times 10^7$ m^{-1} ($\lambda_{SAW} \approx$ 100 nm) and Fermi energies $E_F = 0.376$, 0.381, and 0.403 eV, respectively. This large wavevector value is beyond the state-of-the-art resolution limit of an IDT, so examples in (c)–(e) are just to illustrate the simplified structure in (a) and (b). κ denotes the coupling coefficient between the polariton and the vibrational resonances extracted from equations (8) and (12).

Not only do the TMM and the COM provide similar results for the calculation of the dispersion, but also by solving the COM equation system in Equation (8), a function for the power absorbed by the oscillators can be derived, which can be compared to the extinction plots obtained by the TMM. For this, solutions of the form $x_i = C_i \cdot \exp(i\omega t)$ can be assumed and introduced into the system, solving the equations for C_1 and C_2. From these solutions, the power absorbed by each oscillator can be obtained as

$$\langle P_i \rangle = \frac{1}{T}\int_0^T \mathrm{Re}[F_i \exp(i\omega t)]\mathrm{Re}[\dot{x}_i]dt = \frac{F_1\omega}{2}\mathrm{Im}[C_i]. \quad (11)$$

The optical response of the biosensor is given by the extinction of the heterostructure, defined as $Ext = \frac{R_0 - R}{R_0}$, where R and R_0 designate the power reflected with and without the SAW (i.e. with and without the coupling of the vibrational resonance to the SPPP), respectively. Hence, the SAW, acting as an electrically-controlled virtual diffraction grating, can switch on and off the polariton, unlike in standard systems, such as patterned diffraction gratings, where the polariton is always present. This provides the proposed biosensor with an important advantage since the differential measurement is always made with the analyte already in place for the SAW ON and OFF conditions, instead of standard plasmonic biosensors using patterned gratings, where measurements need to be made before and after placing the analyte (unless the light polarization is rotated, which is a slow process), thus being potentially affected by other effects distinct from the mere analyte. Therefore, since the analyte is present in the calculation of both R and R_0, the extinction can be modelled just as the power transmitted to the SPPP as

$$P_1 \propto \omega \cdot \mathrm{Im}\left[\frac{(\omega_2^2 - i\omega\gamma_2 - \omega^2)A + i\omega\kappa B}{(\omega_1^2 - i\omega\gamma_1 - \omega^2)(\omega_2^2 - i\omega\gamma_2 - \omega^2) - \omega^2\kappa^2}\right]. \quad (12)$$

This power function can be used to fit the extinction curves calculated with the TMM. Fig. 4(c)–(e) present the extinction curves of the CBP/SLG/AlN system calculated by the TMM (red dots) and their fitting to the COM (black curves) for different values of the CBP layer thickness. Both methods show a great agreement, not only when the interaction is strong enough to produce a transparency window within the peak, Fig. 4 (e), but also at weaker coupling, when the only noticeable effect is a broadening of the extinction peak, Fig. 4(d). Furthermore, by using κ as a fitting parameter, the COM allows to extract quantitative information of the coupling even in the absence of a transparency window, thus permitting to monitor the interaction across different coupling regimes.

The benefits of this model for the fingerprinting of organic compounds have been exemplified for CBP on a simple SLG/ALN system, but this methodology can be applied to other substances of biological interest such as thin layers of peptides or proteins on the full biosensor heterostructure. Thus, considering again the original DLG/h-BN/DLG/AlN/Al/AlN system, in Figs. 5 and 6 the COM model is applied to fit the results obtained by the TMM simulations for the biosensor heterostructure covered by ultrathin layers of proteins and peptides, respectively.

Fig. 5 illustrates the biosensor response when coated with a 8-nm thick A/G-IgG protein bilayer. As can be seen in the permittivity curves displayed in Fig. S3 of the Supplementary Information, this protein bilayer presents 2 absorption bands around 1655 cm^{-1} and 1630 cm^{-1}, corresponding to the vibrational resonances of the amide I and amide II groups, respectively.

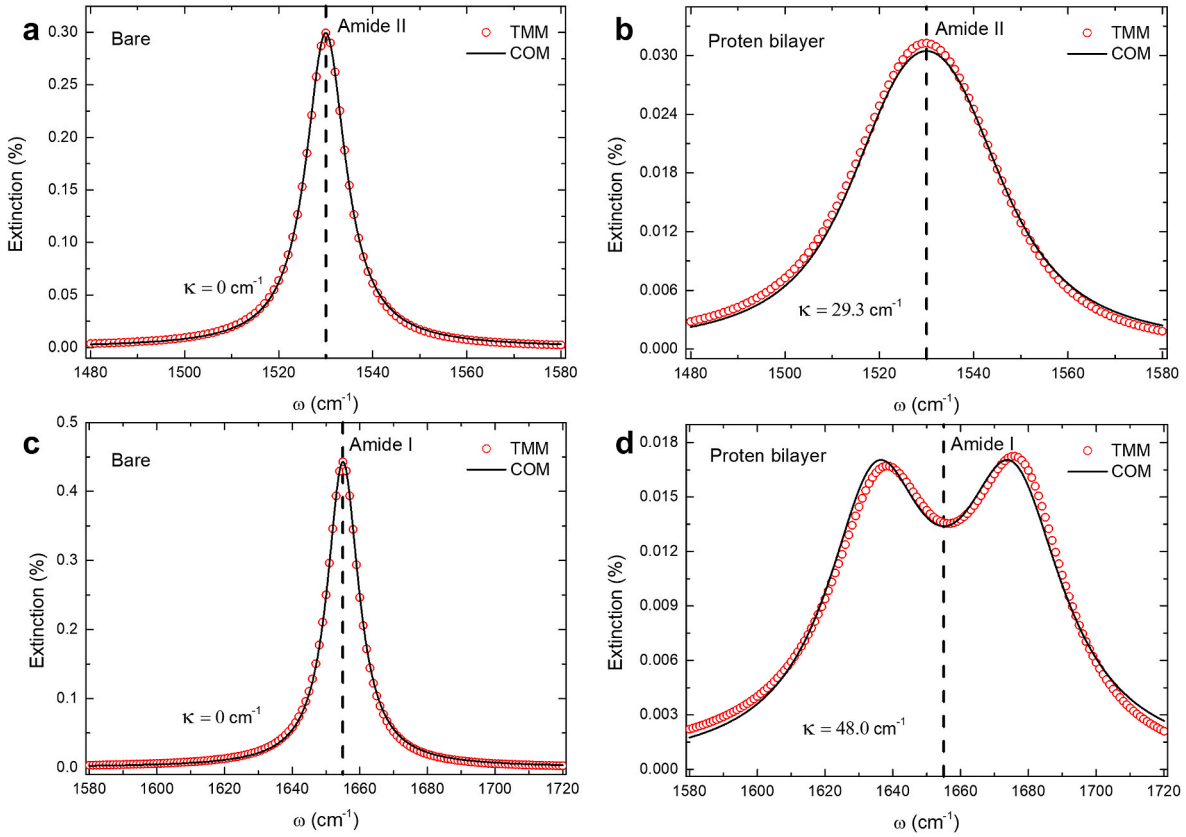

Fig. 5. Response of the biosensor to an A/G-IgG protein bilayer calculated by the TMM (red circles) and the COM (back curve). The comparison of the extinction of the DLG/h-BN/DLG/AlN/Al/AlN heterostructure (a),(c) uncoated and (b),(d) coated with the A/G-IgG protein bilayer indicates the capability of the sensor to fingerprint the protein through its amide I and II bands. The coupling coefficient κ between the polariton and the vibrational resonance is indicated in each case. The polariton wavevector is $k_p = 1.7 \cdot 10^7\ m^{-1}$ ($\lambda_{SAW} \approx 360$ nm) in (a) and (b) and $2.1 \cdot 10^7\ m^{-1}$ ($\lambda_{SAW} \approx 300$ nm) in (c) and (d), whereas the Fermi energy is tuned to E_F = 0.371, 0.386, 0.373, and 0.396 eV in (a), (b), (c), and (d), respectively, in order match the frequency of the polariton with those of the amide bands.

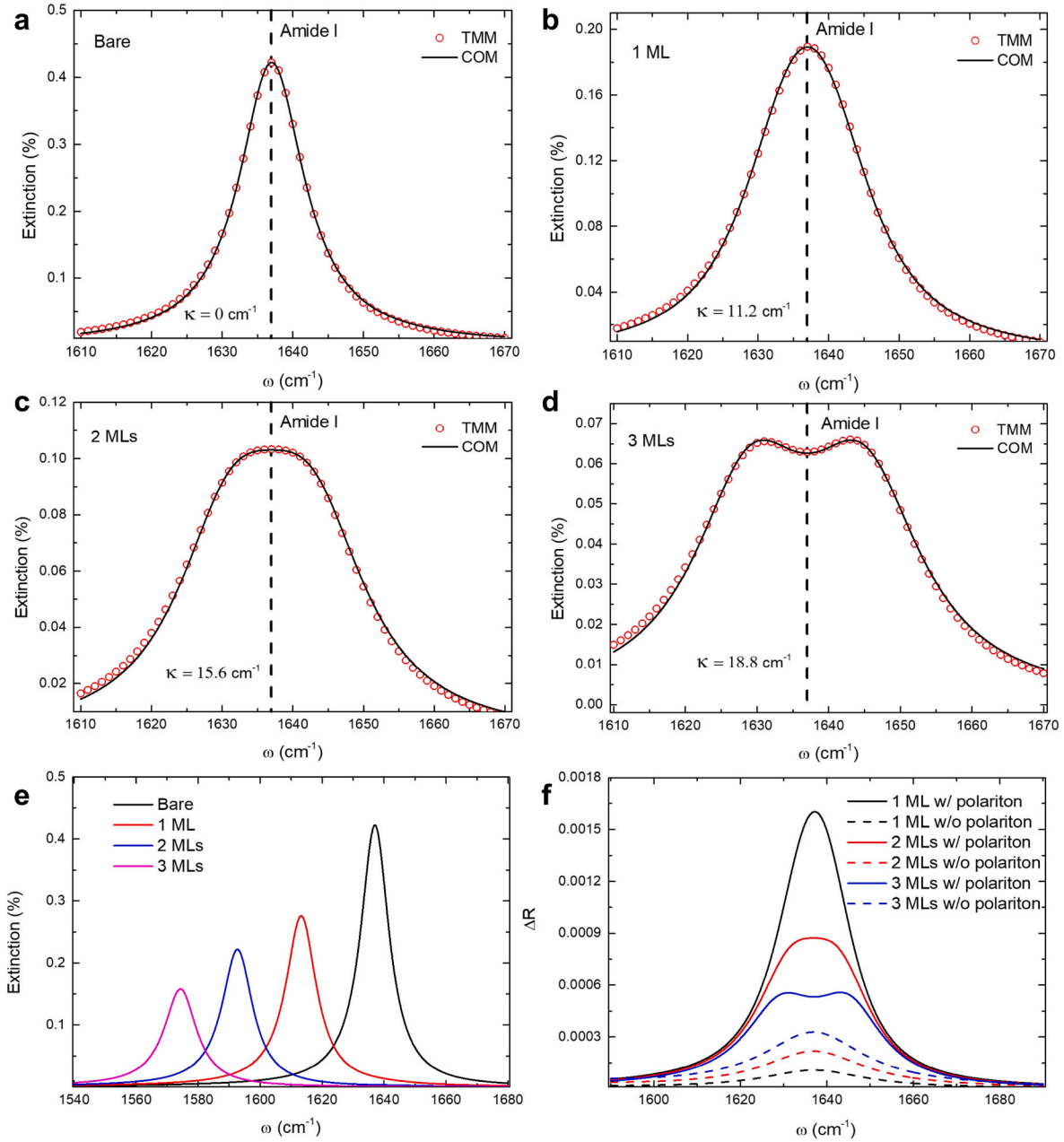

Fig. 6. Response of the biosensor to 1–3 MLs of VGA peptide calculated by the TMM (red circles) and the COM (black curve). The comparison of the extinction of the DLG/h-BN/DLG/AlN/Al/AlN heterostructure (a) uncoated and coated with (b) 1, (c) 2, and (d) 3 MLs of VGA indicates the capability of the sensor to distinguish the three cases unambiguously. In each case, the coupling coefficient κ between the polariton and the vibrational resonance is indicated. The polariton wavevector is $k_p = 2.1 \cdot 10^7$ m^{-1} ($\lambda_{SAW} \approx 300$ nm), whereas the Fermi energy is tuned to $E_F = 0.381$, 0.396, 0.410, and 0.423 eV for the bare sensor and the sensor covered by 1, 2, and 3 MLs of VGA, respectively, in order match the frequency of the polariton with that of the amide I band. (e) Frequency shift in the biosensor response due to the change in the dielectric environment produced by up to 3 MLs of VGA deposited on the sensor surface at a fixed $E_F = 0.381$ eV value. Note that, for fingerprinting, the Fermi level of graphene must be tuned as in (b)–(d), though this shift can be used for quantifying the amount of analyte. (f) Comparison of the change in reflectance ΔR produced in the DLG/h-BN/DLG/AlN/Al/AlN heterostructure (i.e. with polariton) vs in a bare AlN substrate (i.e. without polariton), when both are coated with up to 3 MLs of VGA.

When the protein bilayer is deposited on the device, there is a frequency shift in the SPPP resonance due to the change in the dielectric environment, that can be balanced by gate doping to make the SPPP peak overlap that of the amide group to be sensed. In the case of the amide II, a considerable broadening is observed in the SPPP peak when it is tuned to the frequency of the amide II band, as observed comparing the SPPP in the bare sensor, Fig. 5(a) ($\kappa = 0$), and the SPPP interacting with the resonance of the amide II group in the coated sensor, Fig. 5(b) ($\kappa = 29.3$ cm^{-1}). Conversely, in the case of the amide I band, a transparency window appears within the peak, centred at 1655 cm^{-1}, resulting from a stronger polariton-protein interaction. This is clearly observed comparing the SPPP in the bare sensor, Fig. 5(c) ($\kappa = 0$), and the SPPP interacting with the resonance of the amide I group in the coated sensor, Fig. 5(d) ($\kappa = 48$ cm^{-1}).

Therefore, by fitting to the COM model, the coupling between the vibrational fingerprint and the polariton can be quantified in all cases, allowing to distinguish whether the protein bilayer is present, even in the absence of a transparency window. In this latter case, the presence of the analyte is detected qualitatively as an increase in the width of the extinction peak and quantitatively as a prominent variation of the κ

parameter. It has to be noted that, although the κ parameter has much higher values in the A/G-IgG protein bilayer for both amide groups, as compared to those of the carbazole group of CBP (δ(C–H)$_c$ (see Fig. 4(d)–(e)), the transparency window only appears in the amide I region and not in the amide II. This is because the coupling is not only governed by the rate of energy exchange between oscillators (κ parameter), but also by the relation of this exchange rate and the decay rates of the oscillators (their damping coefficients γ_i). Therefore, since the amide bands are wider (i.e. have larger γ_i) than the vibrational resonances of CBP, a higher κ value is needed to observe a crossover from the initial broadening regime to the subsequent transparency-window regime.

Fig. 6(a)–(d) present the biosensor response in the amide I region when coated with up to three VGA peptide MLs. The extinction spectra show how the SPPP peak broadens gradually as the thickness of VGA is increased up to 2 MLs, whereas a Fano resonance develops for 3 MLs. Again, the COM allows us to quantify the amount of peptide in all cases, confirming that the initial broadening originates from the interaction between the SPPP electric field and the vibrational electric dipole, that later evolves into a transparency window. In all the previous spectra, the frequency shift in the SPPP resonance due to the change in the dielectric environment has been counteracted by gate doping to force the SPPP peak overlap that of the amide I group. Fig. 6(e) shows this frequency shift, that can also be used to quantify the amount of analyte deposited on top of the sensor, as a conventional SPR sensor. Furthermore, this SPR sensor can be complemented by the SAW used as a gravimetric sensor, monitoring the phase shift produced by the mass loading effect. In order to assess the sensitivity of the sensor, Fig. 6(f) depicts the difference in reflectance calculated for the DLG/h-BN/DLG/AlN/Al/AlN heterostructure coated with an increasing number of VGA MLs as compared to that provided by those MLs on a bare AlN substrate without polaritons. It can be pointed out that the polariton enhances the detection signal by approximately 16 times in the ML limit and by 4 times for the 2-ML case. This provides a powerful tool for assessing VGA, both as a ML and a bilayer, the latter being specially interesting as it forms ion channels that allow conduction of monovalent cations through lipid membranes.

It has to be noted that all the presented results have been obtained for a graphene mobility value of 10000 $cm^2V^{-1}s^{-1}$, which is a conservative assumption considering that state-of-the-art CVD graphene can exhibit mobility values up to 70000 $cm^2V^{-1}s^{-1}$ at room temperature (Fazio et al., 2019). Therefore, an improved biosensor performance can be achieved just by using better quality graphene, as discussed in Section 4 of the Supplementary Information. Moreover, the sensitivity of the biosensors might be enhanced by enabling an alternated in-phase and out-of-phase modulation of the optical excitation and the RF signal fed to the IDT for creating the SAW. This method, which strongly suppresses the influence of thermal or laser power fluctuations, allows to increase the signal to noise ratio (Fandan et al., 2020). Furthermore, the proposed plasmonic biosensor paves the way for the development of advanced SAW-assisted LOC systems combining the chemical fingerprinting capability of this novel sensor with complementary SAW-mediated physical sensing mechanisms (Ballantine, 1997) and SAW-driven microfluidic capabilities (droplet streaming, mixing, etc) (Ding et al., 2013; Wixforth, 2003) previously reported in the literature. In a different approach, the proposed biosensor could be adapted to work in a liquid environment by using an AlN crystal orientation providing a shear-horizontal SAW (Love mode) instead of a sagittal SAW (Rayleigh mode) (Hu et al., 2007) or even combining both at different in-plane propagation directions (Kobayashi et al., 1995).

4. Conclusions

We have theoretically demonstrated a novel plasmonic biosensor where the local dynamic modulation of the active surface induced by an on-chip electrically-controlled surface acoustic wave resonator acts as a virtual diffraction grating allowing to couple far-field light into propagating surface polaritons without any patterning. A TMM-tailored gated graphene-based van der Waals heterostructure permits to generate and tune surface plasmon-phonon polaritons accross the mid-infrared range covering the vibrational resonances of most organic compounds. The device has been theoretically investigated for fingerprinting ultrathin biolayers via SEIRA spectroscopy, proving its sensitivity down to the ML limit. The plasmonic response of the acoustically-rippled surface has been tested with various analytes, including thin films (down to a ML) of CBP, an organic semiconductor with sharp and intense absorption lines, as well as biological compounds with broad and weak absorption bands such as A/G-IgG protein bilayers and VGA peptide MLs. The COM analysis demonstrates that the biosensor response is able to elucidate the presence of extremely thin analyte layers in all cases, even when a faint interaction between the vibrational resonances of the molecules and the polaritons does not lead to a Fano resonance but only to a resonance broadening.

CRediT authorship contribution statement

Raúl Izquierdo-López: Conceptualization, Methodology, Data curation, Formal analysis, Investigation, Software, Validation, Visualization, Writing – original draft. **Rajveer Fandan:** Methodology, Software, Writing – review & editing. **Alberto Boscá:** Resources, Writing – review & editing. **Fernando Calle:** Writing – review & editing, Funding acquisition, Project administration. **Jorge Pedrós:** Conceptualization, Methodology, Visualization, Writing – original draft, Funding acquisition, Project administration, Supervision.

Declaration of competing interest

The authors declare that they have no known competing financial interests or personal relationships that could have appeared to influence the work reported in this paper.

Data availability

Data will be made available on request.

Acknowledgements

This work has received funding from the Spanish Ministry of Science and Innovation (MICINN) through project 2D-SAWNICS (PID2020-120433GB-I00). We also acknowledge support from project NMAT2D-CM (P2018/NMT-4511) funded by Comunidad de Madrid, as well as project MAD2D-CM-UPM (MRR Materiales Avanzados-UPM1) funded by Comunidad de Madrid, the Recovery, Transformation and Resilience Plan, and NextGenerationEU from the European Union. R.I.-L. acknowledges financial support from the Universidad Politécnica de Madrid (Ayudas para contratos predoctorales, Programa propio de I+D+i 2020).

Appendix A. Supplementary data

Supplementary data to this article can be found online at https://doi.org/10.1016/j.bios.2023.115498.

References

Adato, R., Altug, H., 2013. Nat. Commun. 4, 2154.
Autore, M., Li, P., Dolado, I., Alfaro-Mozaz, F.J., Esteban, R., Atxabal, A., Casanova, F., Hueso, L.E., Alonso-González, P., Aizpurua, J., Nikitin, A.Y., Vélez, S., Hillenbrand, R., 2018. Light Sci. Appl. 7, 17172.
Ballantine, D.S., 1997. Acoustic Wave Sensors. Acad. Press, San Diego.
Barth, A., 2007. Biochim. Biophys. Acta Bioenerg. 1767, 1073–1101.
Brar, V.W., Jang, M.S., Sherrott, M., Kim, S., Lopez, J.J., Kim, L.B., Choi, M., Atwater, H., 2014. Nano Lett. 14, 3876–3880.
Brar, V.W., Jang, M.S., Sherrott, M., Lopez, J.J., Atwater, H.A., 2013. Nano Lett. 13, 2541–2547.

Dai, S., Fei, Z., Ma, Q., Rodin, A.S., Wagner, M., McLeod, A.S., Liu, M.K., Gannett, W., Regan, W., Watanabe, K., Taniguchi, T., Thiemens, M., Dominguez, G., Neto, A.H.C., Zettl, A., Keilmann, F., Jarillo-Herrero, P., Fogler, M.M., Basov, D.N., 2014. Science 343, 1125–1129.
Ding, X., Li, P., Lin, S.C.S., Stratton, Z.S., Nama, N., Guo, F., Slotcavage, D., Mao, X., Shi, J., Costanzo, F., Huang, T.J., 2013. Lab Chip 13, 3626–3649.
Fandan, R., Pedrós, J., Calle, F., 2021. ACS Photonics 8, 1698–1704.
Fandan, R., Pedrós, J., Hernández-Mínguez, A., Iikawa, F., Santos, P.V., Boscá, A., Calle, F., 2020. Nano Lett. 20, 402–409.
Fandan, R., Pedrós, J., Schiefele, J., Boscá, A., Martínez, J., Calle, F., 2018. J. Phys. D Appl. Phys. 51, 204004.
Fang, Z., Wang, Y., Schlather, A.E., Liu, Z., Ajayan, P.M., García de Abajo, F.J., Nordlander, P., Zhu, X., Halas, N.J., 2014. Nano Lett. 14, 299–304.
Fazio, D.D., Purdie, D.G., Ott, A.K., Braeuninger-Weimer, P., Khodkov, T., Goossens, S., Taniguchi, T., Watanabe, K., Livreri, P., Koppens, F.H.L., Hofmann, S., Goykhman, I., Ferrari, A.C., Lombardo, A., 2019. ACS Nano 13, 8926–8935.
Fei, Z., Andreev, G.O., Bao, W., Zhang, L.M., McLeod, A.S., Wang, C., Stewart, M.K., Zhao, Z., Dominguez, G., Thiemens, M., Fogler, M.M., Tauber, M.J., Castro-Neto, A. H., Lau, C.N., Keilmann, F., Basov, D.N., 2011. Nano Lett. 11, 4701–4705.
Friedt, J.M., Francis, L., Reekmans, G., Palma, R.D., Campitelli, A., Sleytr, U.B., 2004. J. Appl. Phys. 95, 1677–1680.
Friedt, J.M., Francis, L.A., 2016. Sens. Bio-Sens. Res. 11, 60–70.
Galopin, E., Beaugeois, M., Pinchemel, B., Camart, J.C., Bouazaoui, M., Thomy, V., 2007. Biosens. Bioelectron. 23, 746–750.
Hu, G., Xu, J., Auner, G.W., Smolinski, J., Ying, H., 2007. Electron. Lett. 43, 1006–1007.
Hu, H., Yang, X., Zhai, F., Hu, D., Liu, R., Liu, K., Sun, Z., Dai, Q., 2016. Nat. Commun. 7, 12334.
Huck, C., Neubrech, F., Vogt, J., Toma, A., Gerbert, D., Katzmann, J., Härtling, T., Pucci, A., 2014. ACS Nano 8, 4908–4914.
Ju, L., Geng, B., Horng, J., Girit, C., Martin, M., Hao, Z., Bechtel, H.A., Liang, X., Zettl, A., Shen, Y.R., Wang, F., 2011. Nat. Nanotechnol. 6, 630–634.
Kamenetskii, E., Sadreev, A., Miroshnichenko, A., 2018. In: Fano Resonances in Optics and Microwaves, vol. 219. Springer.
Kazan, M., Pereira, S., Correia, M., Masri, P., 2009. J. Appl. Phys. 106, 023523, 10.
Kobayashi, Y., Tanaka, N., Okano, H., Takeuchi, K., Usuki, T., Shibata, K., 1995. Jpn. J. Appl. Phys. 34, 2668–2673.
Lean, E.G., 1973. In: Wolf, E. (Ed.), Progress in Optics, vol. XI. Elsevier.
Lee, I.H., Yoo, D., Avouris, P., Low, T., Oh, S.H., 2019. Nat. Nanotechnol. 14, 313–319.
Li, Y., Yan, H., Farmer, D.B., Meng, X., Zhu, W., Osgood, R.M., Heinz, T.F., Avouris, P., 2014. Nano Lett. 14, 1573–1577.
Liu, N., Langguth, L., Weiss, T., Kästel, J., Fleischhauer, M., Pfau, T., Giessen, H., 2009. Nat. Mater. 8, 758–762.
Low, T., Avouris, P., 2014. ACS Nano 8, 1086–1101.
López-Lorente, A.I., Mizaikoff, B., 2016. Anal. Bioanal. Chem. 408, 2875–2889.
Neuman, T., Huck, C., Vogt, J., Neubrech, F., Hillenbrand, R., Aizpurua, J., Pucci, A., 2015. J. Phys. Chem. C 119, 26652–26662.
Nikitin, A.Y., Alonso-González, P., Hillenbrand, R., 2014. Nano Lett. 14, 2896–2901.
Renaudin, A., Chabot, V., Grondin, E., Aimez, V., Charette, P.G., 2010. Lab Chip 1, 111–115.
Rodrigo, D., Limaj, O., Janner, D., Etezadi, D., Garcia de Abajo, F.J., Pruneri, V., Altug, H., 2015. Science 349, 165–168.
Rodrigo, D., Tittl, A., Limaj, O., Abajo, F.J.G.d., Pruneri, V., Altug, H., 2017. Light Sci. Appl. 6, e16277.
Ruppert, C., Neumann, J., Kinzel, J.B., Krenner, H.J., Wixforth, A., Betz, M., 2010. Phys. Rev. B Condens. Matter 82, 081416.
Schiefele, J., Pedrós, J., Sols, F., Calle, F., Guinea, F., 2013. Phys. Rev. Lett. 111, 237405.
Schwaighofer, A., Brandstetter, M., Lendl, B., 2017. Chem. Soc. Rev. 46, 5903–5924.
Sonato, A., Agostini, M., Ruffato, G., Gazzola, E., Liuni, D., Greco, G., Travagliati, M., Cecchini, M., Romanato, F., 2016. Lab Chip 16, 1224–1233.
Vogt, J., Huck, C., Neubrech, F., Toma, A., Gerbert, D., Pucci, A., 2015. Phys. Chem. Chem. Phys. 17, 21169–21175.
Wixforth, A., 2003. Superlattice. Microst. 33, 389–396.
Yi, J., You, E.M., Ding, S.Y., Tian, Z.Q., 2020. Natl. Sci. Rev. 7, 1228–1238.
Zhan, T., Shi, X., Dai, Y., Liu, X., Zi, J., 2013. J. Phys. Condens. Matter 25, 215301.
Zhang, N., Luo, W., Wang, L., Fan, J., Wu, W., Ren, M., Zhang, X., Cai, W., Xu, J., 2022. Nat. Commun. 13, 983.
Zhao, Y., Hu, X., Chen, G., Zhang, X., Tan, Z., Chen, J., Ruoff, R.S., Zhu, Y., Lu, Y., 2013. Phys. Chem. Chem. Phys. 15, 17118.